ORNL/SPR-2024/3482

Report on DIC Cyclic Dryout Testing of ATF Cladding Materials

Mackenzie Ridley
Samuel Bell
Jennifer Espersen
Nathan Capps

July 2024

OAK RIDGE National Laboratory

ORNL IS MANAGED BY UT-BATTELLE LLC FOR THE US DEPARTMENT OF ENERGY

ORNL/M3FT-24OR020204043

DOE Advanced Fuels Campaign

REPORT ON DIC CYCLIC DRYOUT TESTING OF ATF CLADDING MATERIALS

Mackenzie Ridley
Samuel Bell
Jennifer Espersen
Nathan Capps

July 2024

Prepared by
OAK RIDGE NATIONAL LABORATORY
Oak Ridge, TN 37831
managed by
UT-BATTELLE LLC
for the
US DEPARTMENT OF ENERGY
under contract DE-AC05-00OR22725

ACRONYMS AND ABBREVIATIONS

AOO	Anticipated Operational Occurrence
BWR	Boiling Water Reactor
CDO	Cyclic Dryout
DAQ	Digital Acquisition System
DNB	Departure from Nucleate Boiling
ORNL	Oak Ridge National Laboratory
SATS	Severe Accident Test Station
Zry2	Zircaloy-2
Zry4	Zircaloy-4

CONTENTS

ABSTRACT

Boiling water reactors can experience anticipated operational occurrences, where an expected deviation from normal operating conditions is witnessed for short time scales. One example of such transients arises from cladding dryout, where stable boiling becomes unstable, resulting in cladding heat up before re-wetting occurs. To understand the impact of such transients on fuel cladding lifetime and performance, cyclic dryout conditions were imposed upon fresh fuel cladding in the absence of irradiation. Pressurized cladding tube segments were exposed to rapid temperature increases to intermediate temperatures below a cladding rupture threshold and deformation was monitored *in situ* via 3-D digital image correlation. The impact of cycle frequency on cladding deformation was assessed. A clear understanding of elastic and plastic strain responses were developed for Zr alloy deformation under temperature transients, and these results can be used to support material model development and validate fuel performance codes.

1. Introduction

Anticipated operational occurrences (AOOs) are transient events that occur during normal operation of a nuclear power plant and are expected to happen one or more times throughout the plant's operational lifetime [1]. Unlike design basis accidents, AOOs are managed so that fuel failure does not occur, and the fuel is expected to return to service afterward. In the context of Boiling Water Reactors (BWRs) and Pressurized Water Reactors (PWRs), fuel rod failure during an AOO is assessed by criteria such as dryout or departure from nucleate boiling (DNB). The U.S. nuclear industry has recently initiated efforts to uprate power plants, which reduces margins to dryout or DNB. This may necessitate additional considerations or new criteria specific to cladding to safely and economically enhance nuclear reactor capabilities. The Japanese Atomic Energy Society has found that Zircaloy cladding can be reused after a simulated AOO if the cladding remains below 1073 K for 100 seconds [2,3], suggesting a potential avenue for consideration within the U.S. community. However, AOO events in PWRs are generally quite aggressive and may require further research and development in thermal hydraulics and cladding materials. Conversely, BWRs could potentially benefit immediately if a cladding-specific criterion can be established.

BWRs operate under stable boiling conditions where the thermal hydraulic state keeps the fuel cladding temperature constant. However, an AOO can cause dryout, where stable boiling is disrupted, and the cladding temperature rapidly increase before re-wetting occurs. Other AOOs may involve cyclic changes where the coolant shifts between stable boiling and an over-moderated state, leading to steam flashing and re-wetting. One of the most severe cyclic AOOs in BWRs is the Anticipated Transient Without Scram (ATWS), which occurs due to reactor power oscillations when an automatic reactor scram fails to activate. This failure can destabilize the coolant, transitioning it from stable to unstable boiling conditions due to fluctuating power levels. Under certain conditions, failure to scram during ATWS can escalate a minor event into a more severe accident, directly impacting fuel performance and increasing the risk of cladding failure. As reactor and coolant conditions oscillate, the cladding temperature undergoes rapid fluctuations, leading to dryout and subsequent cooling when the cladding re-wets. Such thermal cycles can compromise the structural integrity of the fuel cladding, potentially causing failure during the event or in post handling of the impacted fuel.

Dryout events in BWRs are exemplified by incidents at LaSalle County-2 and Oskarshamn-2 nuclear power plants [4,5]. At LaSalle Unit 2, a dual recirculation pump trip caused excessive neutron flux oscillations, leading to power fluctuations every 2 to 3 seconds with a 25% increase and decrease relative to steady-state power. Fortunately, reactor operators detected the event, and the reactor automatically shut down approximately eight minutes after the incident began. Subsequent analysis revealed that fuel peaking factors increased from 2.11 to 2.65, approaching fuel thermal mechanical limits. More recently, Oskarshamn-2 encountered a loss of feedwater pre-heaters combined with a failure

in control system logic, resulting in the injection of cooler water into the reactor core and causing over-moderation and increased power. This imbalance led to power oscillations in the core. Once again, automatic reactor scramming averted damage to the reactor and fuel. TRACE/SIMULATE-3K analysis of the event indicated that power oscillations were escalating until the high-power condition triggered the reactor scram [6]. A critical distinction between these events and an ATWS is that both reactors automatically scrammed. However, in both cases, if the reactors had failed to shut down, continued power escalation could have eventually led to fuel failure.

The Japanese Atomic Energy Society determined that Zircaloy cladding can be reused after dryout as long as the cladding remained below 1073 K for 100 seconds [2,3]. While the U.S. BWR reactor fleet currently defines dryout as indication that fuel cladding must be removed from service, With the recent industry initiative to pursue extend power uprates in conjunction with plans to extend the peak rod average burnup, it may become critical to refine safety margins. Such a change would require a transition away from a thermal hydraulic reuse criteria to a to a cladding performance-based reuse criterion. In support of such efforts, cyclic dryout events were simulated at Oak Ridge National Laboratory's (ORNL) Severe Accident Test Station (SATS) to assess cladding deformation in situ throughout a temperature cycling event. Demonstration of cyclic dryout testing has previously been reported [7], although deformation was limited to post-test strain analysis via calipers. Currently, stereo digital image correlation (DIC) was employed to track elastic and plastic response of pressurized cladding tube segments during the cyclic dryout tests. Zircaloy-4, Zircaloy-2, and FeCrAl cladding segments were compared to assess material performance and provide insights for development of a cladding performance-based reuse criteria through separate effects testing.

2. Methodology

2.1 Test Setup

The Severe Accident Test Station was used to perform cyclic dryout experiments with in situ strain monitoring. A 4-lamp infrared heating furnace was used to simulate dryout conditions up to 750°C. Similar experiments have been performed without strain monitoring and additional details on the setup can be found here [7].

The specimens were connected to a high-pressure line with Swagelok fittings with the bottom end of the sample free hanging in the furnace. Pressure was supplied inside the cladding tube and maintained with connection of a gas cylinder, making pressure a constant variable throughout testing. The sample was placed in the furnace within a quartz tube such that steam could be flown around the exterior of the sample. Specimens were heated to 100°C in air, upon which steam was injected into the furnace. Upon establishing stable steam flow, the specimen was heated from 100°C to 750°C at a target heating rate of 15°C/s. Once the maximum temperature was reached, the furnace was air cooled to 300°C in ~3.5 minutes. Then, consecutive cycles were performed from 300 – 750°C.

Thermocouples were positioned on the front side of the cladding, where specimen images were collected during testing. The control thermocouple was 1 inch above the cladding centerline, Limit was placed 1 inch below cladding centerline, and two additional TCs (upper and lower) were placed to monitor temperature 2 inches above and below cladding centerline.

2.2 Specimens

A 6" stress relief annealed Zircaloy-4 cladding segment was exposed to cyclic conditions at 6.31 MPa internal pressure for 36 cycles. Then, a 6" C26M2 FeCrAl alloy tube was exposed to the cyclic conditions with an internal pressure of 3.9 MPa. Finally, a 6" Zircaloy-2 cladding segment was exposed to cyclic conditions at 9.25 MPa. The Zry-2 specimen represented a realistic material type to undergo dryout conditions as the primary BWR cladding candidate. The specimen geometries can be found on

Table 1, where comparable initial applied hoop stresses were between 45 – 49 MPa for all three materials. Hoop stress was calculated using the thin-walled approximation shown in Equation 1;

$$\frac{PD}{2h} \quad (1)$$

Where P is the internal cladding pressure (MPa), D is the midpoint cladding diameter at a given testing time, and h is the cladding wall thickness. The cladding midpoint diameter and the wall thickness can be corrected for during testing where strain evolution is evident, Equations 2 and 3;

$$D = D_i * (1 + \epsilon_{xx}) \quad (2)$$

$$h = h_i * (1 - \epsilon_{xx}) \quad (3)$$

Here, D_i and h_i are the initial diameter and wall thickness values, and ϵ_{xx} represents the hoop strain at a given point in time that is experienced by the cladding. *In situ* hoop direction strain measurements allow for an approximation of the cladding hoop stress during temperature cycling.

Table 1. Sample geometries used for testing.

Cladding Tube Material	Outer Diameter (mm)	Wall Thickness (mm)	Internal Pressure (MPa)	Initial Hoop Stress (MPa)
Zircaloy-4	9.5	0.575	6.3	49
C26M2 FeCrAl	10.28	0.43	3.9	45
Zircaloy-2	12.3	1.15	9.25	45

2.3 Digital Image Correlation

Two 4-megapixel cameras with blue light filters were positioned in view of the specimens with ~10° stereo angle to capture deformation [8]. Specimens were painted with a high-temperature white base paint and black speckle patterns to allow for pixel tracking. Cameras were calibrated with both a reference grid and a reference undeformed paint speckle pattern prior to testing. During the experiments, images were captured at 5 frames per second until rupture or until the test was stopped. Temperature and pressure readouts were connected to the camera system through a digital acquisition system such that each captured image had an associated time, temperature, and pressure value. Analysis was performed with Hencky strain calculations and tube edges were removed from analysis to prevent edge artifacts.

3. Results

3.1 Alumina Thermal Expansion Validation

The test conditions (i.e. steam flow, rapidly changing light exposure, quartz lab ware between the sample and cameras) are not considered ideal for high resolution image capture with digital image correlation, and as a result of such factors, high noise is often witnessed within the data. Yet, clear trends can still be retained through the current setup, such as tracking thermal expansion of materials. Figure 1 shows strain analysis results from establishing a region of interest (Figure 1a) on the alumina thermocouple rod. The thermocouple rod is not pressurized, so all measured strains are assumed noise and thermoelastic response. While the thermocouple rod is not perfectly centered in the furnace and is free hanging in the gas stream and thus more susceptible to vibrations than the heavier cladding specimen, we see an increase in strain as temperature increases. Despite the high noise, a linear fit was applied to the data (red curve, Figure 1b) to showcase a thermal expansion coefficient of ~9×10^{-6} /°C. This agrees well with the known CTE of α-alumina (blue dotted line) which validates that thermal expansion can indeed be measured within the highest noise regions of our datasets. This validation permits CTE measurements on this cladding sample during cycling, discussed later.

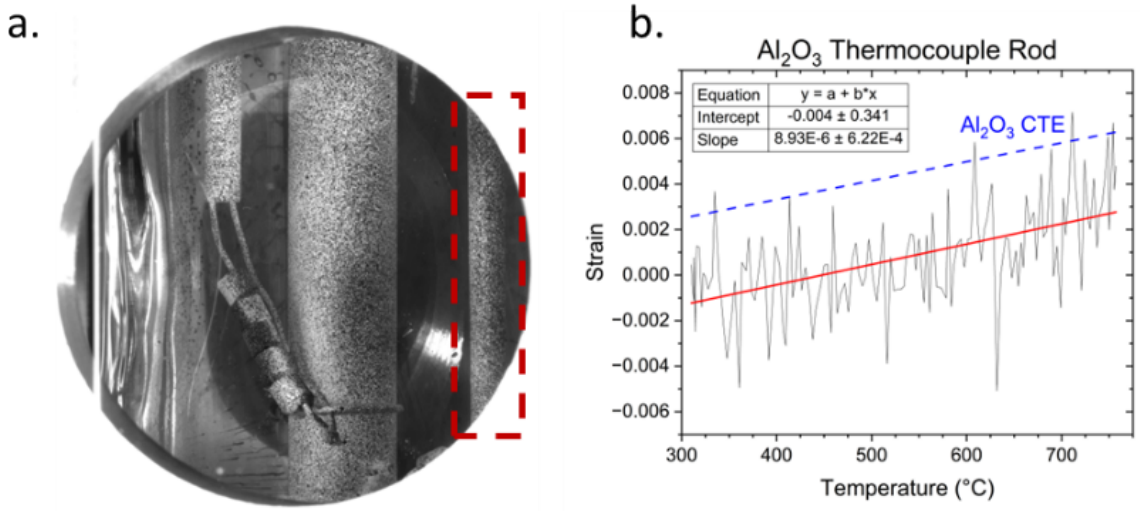

Figure 1. Image of Run 3 with red box showcasing Al_2O_3 thermocouple sheath used for analysis, b. average elastic strain of thermocouple rod for one heating cycle compared to literature CTE of Al_2O_3.

3.2 Zry-4 CDO Test with 49 MPa Hoop Stress

Figure 2a shows the temperature and pressure profiles of Zry4 CDO test with initial 49 MPa hoop stress, and Figure 2b shows only the first three cycles. There is temperature variation between the thermocouples due to the higher heating rate used for the test compared to 5°C/s heating rate tests performed in the past on the same furnace [8]. A temperature difference of 29±22°C was found throughout testing, where the highest temperature gradient difference comes during the heating event at 750°C. A tube pressure leak was recorded during testing, which was accounted for during the test with a slight pressure increase at ~5,000s. Thus, the pressure leak stayed within 0.36 MPa of the initial pressurization value and averaged 6.21±0.07 MPa. The control thermocouple, closest to the DIC region of interest, was used for image analysis. The cladding did not rupture after the full 36 cycles of exposure. The CDO test lasted ~148 minutes in total with constant steam flow, although only ~31 minutes of that time consisting of the sample temperature being greater than 450°C.

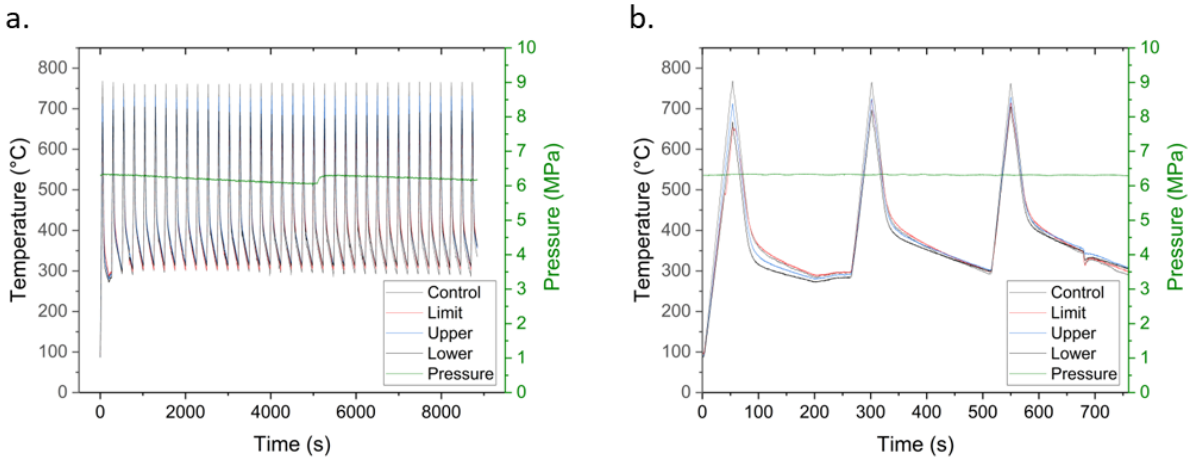

Figure 2. a. Full temperature and pressure history for Test 4, b. temperature and pressure history for first three cycles.

Uniform deformation occurred for the majority of the test. However, posttest diametric strain analysis (Figure 3a) indicated that the cladding began experiencing non uniform deformation after the 36 cycles of exposure. The top of the cladding experienced high hoop strains on the order of 12% (outside

the view field for DIC), while the bottom of the cladding strained only ~2%. The region of interest for image collection by DIC is highlighted in red for reference. Post test, a clear change in strain evolution was witnessed, which was captured during testing by DIC as well, in Figure 3b after 17 thermal cycles. The general deformation profile associated with the sample agrees with the thermocouple temperatures, where the top of the sample was generally hotter during temperature cycling. This nonuniform strain profile appeared in the DIC data after ~4 cycles, where initial cycles showed uniform straining profiles. This was likely due to the low strain levels associated with the start of testing. Post test, the high-temperature paint remained in good contact with the cladding, Figure 3c, ensuring that the collected data from the speckle pattern was reflecting the deformation of the cladding substrate.

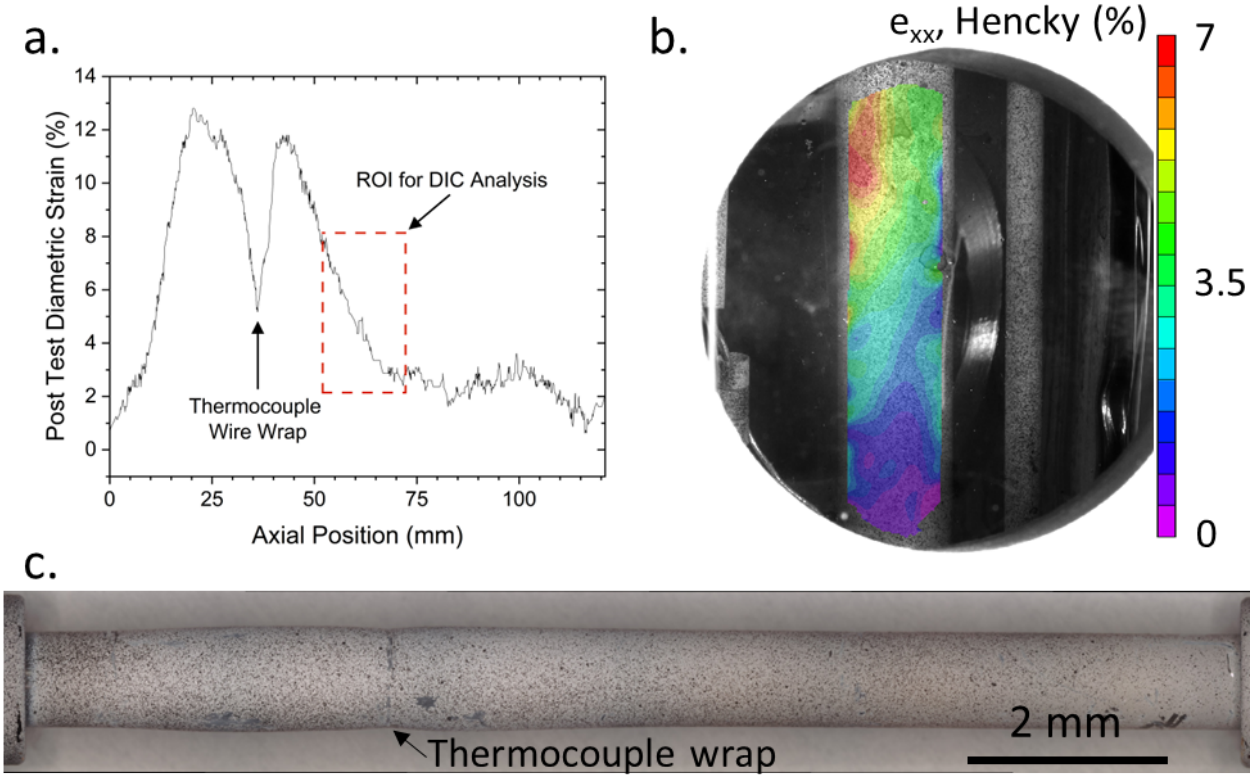

Figure 3. a. Post Test strain analysis of Zry-4 cladding, b. representative strain accumulation image after 17 thermal cycles, and c. optical image of tube after testing.

The hoop strain profile for the full Zry-4 test is shown in Figure 4a and the initial cycle strain evolution is shown in Figure 4b. Data presented was averaged from the full map collected at each timestamp during testing in order to collect representative strain data from all visible camera pixels. Strain oscillations were witnessed upon heating and cooling cycles, with a total strain increase after each cycle. Figure 4b shows the discontinuity in strain at ~730°C, where there is a sharp increase in deformation upon heating. Cycle 21 was removed from the dataset due to order of magnitude size error, associated with water droplets falling down the tube and back into view of the camera which prevented collection of reliable images of the specimen.

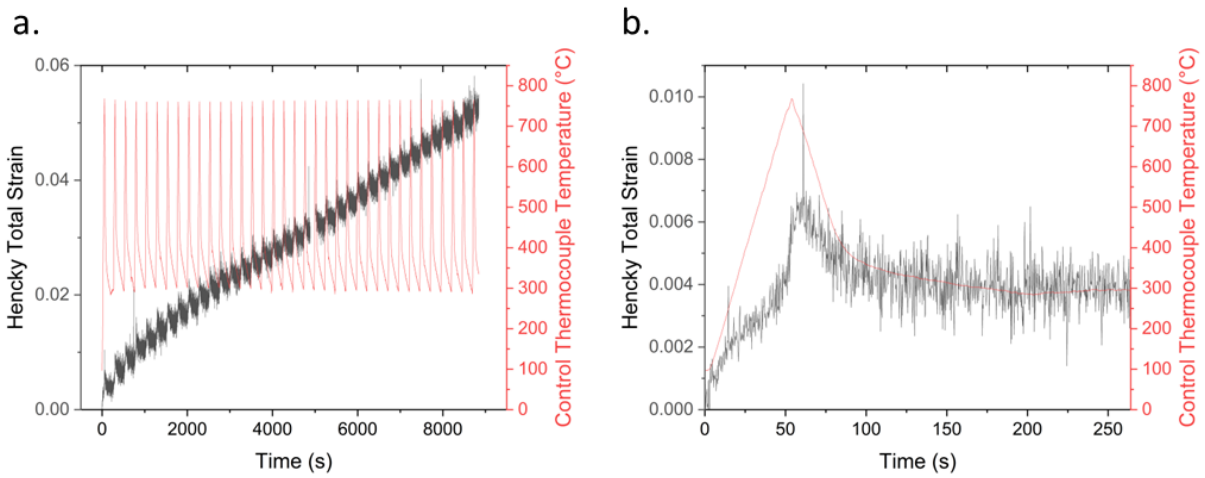

Figure 4. Averaged strain evolution of Zry-4 for a. full test and b. first cycle.

The elastic response captured within the total strain data from Figure 4 was removed by dispersing the data in to heating and cooling cycles. Figure 5a shows the heating cycle strains and Figure 5b shows the cooling cycle strains up to 36 cycles. Coefficients of thermal expansion (CTEs) were calculated upon heating (up to 700°C) and upon cooling (from 700-400°C). Data above 700°C was not used to ensure that high-temperature plastic deformation was not included in the thermal expansion calculation. Data below 400°C was not included upon cooling due to the high number of images collected at the lower temperatures, associated with the longer exposure time during air cooling. Cycle 21 was removed upon heating and cycles 19 & 20 were removed upon cooling due to unrealistic noise levels.

CTE values for each cycle upon heating and cooling are shown in Figure 5 (c,d), compared to Zry-4 data used in BISON (red) [9] and Zr alloy data from MatLIB (blue) [10]. While a wide scatter exists, the results prove that 3D DIC in a complex IR heating steam flow environment can measure thermal expansion of Zr tubes. The average CTE was 5.64×10^{-6} /°C and 5.88×10^{-6} /°C upon heating and cooling, respectively, which agree with both the BISON and MatLIB models, and given enough statistics, this approach could be used to refine and reduce the uncertainties associated with those models as well as to be more specific to the cladding type (i.e. chemistry, manufacturing, and heat treatment effects on hoop direction CTE of cladding tubes).

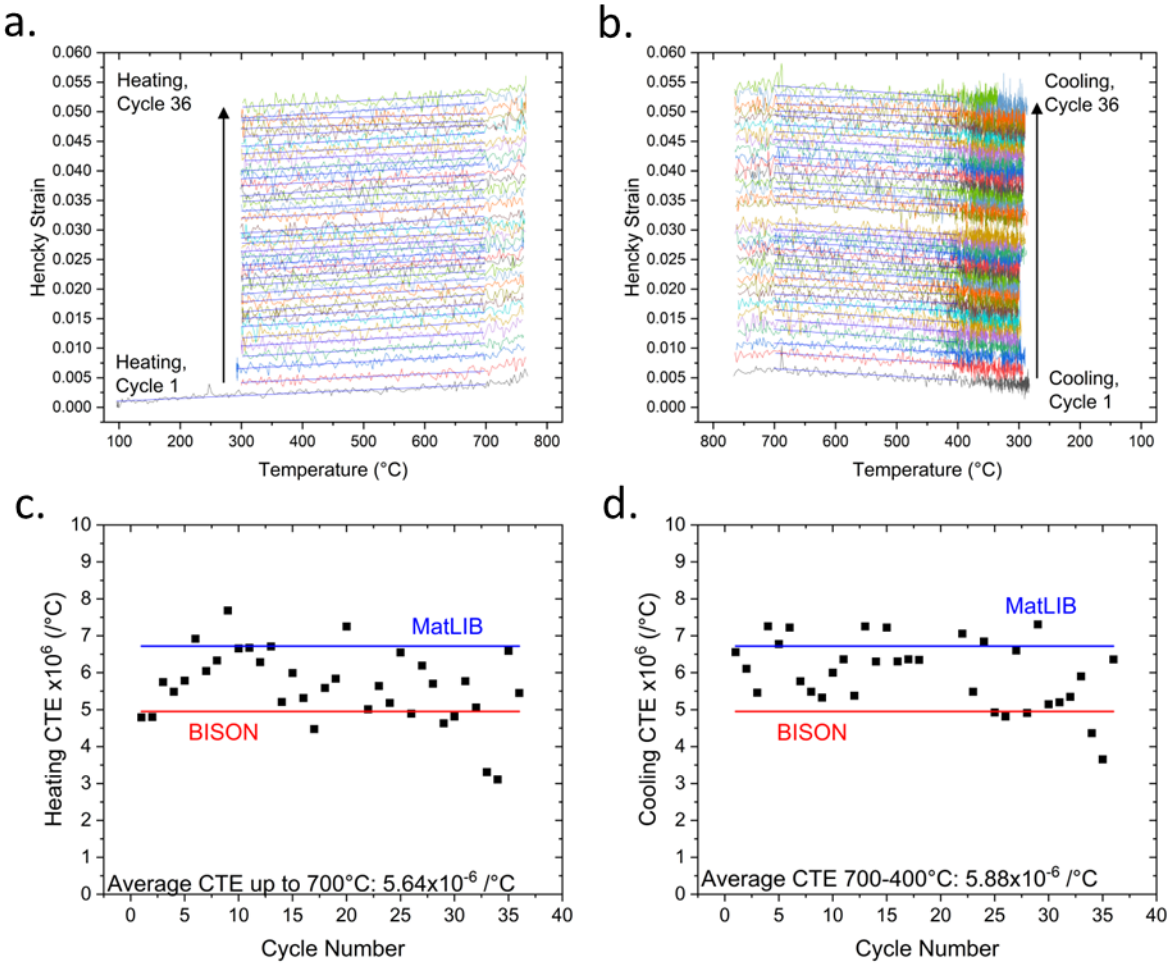

*Figure 5. Strain profiles on heating (a) and cooling (b), thermal expansion calculation on heating up to 700°C (c) and on cooling from 700 - 400°C. * Cycle 21 was removed upon heating and cycles 19 and 20 were removed upon cooling due to high noise.*

The calculated CTEs upon heating for each cycle were subtracted from the total strain at each cycle such that only plastic strains from each cycle event remain (Figure 6). The presented total plastic strain was accumulated over the entirety of each heating and cooling cycle. Clear evidence of strain hardening is found within the first 5 cycles for Zry-4. A linear fit was applied to the total plastic strain as a function of time for cycles 7-36 and a steady state strain rate of 5.087×10^{-6} /s^{-1} was calculated.

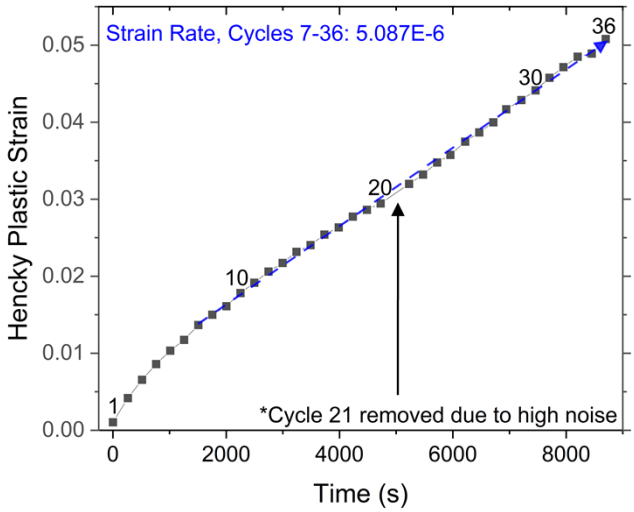

*Figure 6. Plastic strain accumulation over each cycle after thermal expansion elastic strains were subtracted from data. * Cycle 21 was removed due to high noise.*

Utilizing hoop direction creep data by Bell et al (Figure 7a), best fit lines were used to calculate the temperature dependence strain rates for Zry-4 with ~49 MPa hoop stress. The temperature dependent hoop strain rate for this stress level is shown in Figure 7b (black squares with trend line). Deformation below 450°C was assumed negligible during cyclic dryout testing for Zry-4 with 51 MPa hoop stress due to a calculated strain rate on the order of $1x10^{-8}$ $/s^{-1}$ at ~450°C. Ignoring sample exposure time below 450°C, an average specimen temperature of 579°C was calculated over all 36 cycles. This average sample temperature was used to plot the cyclic dryout plastic strain rate alongside literature creep data trends, where good agreement was found. Thus, the results imply that plastic deformation during transients can be predicted and summarized by their average surface temperature during the transient. Likely, instances such as variable internal pressure or exceeding the Zr phase change temperature would induce new strain rate trends that would require a full analysis of the cladding transient history rather than an average temperature approximation.

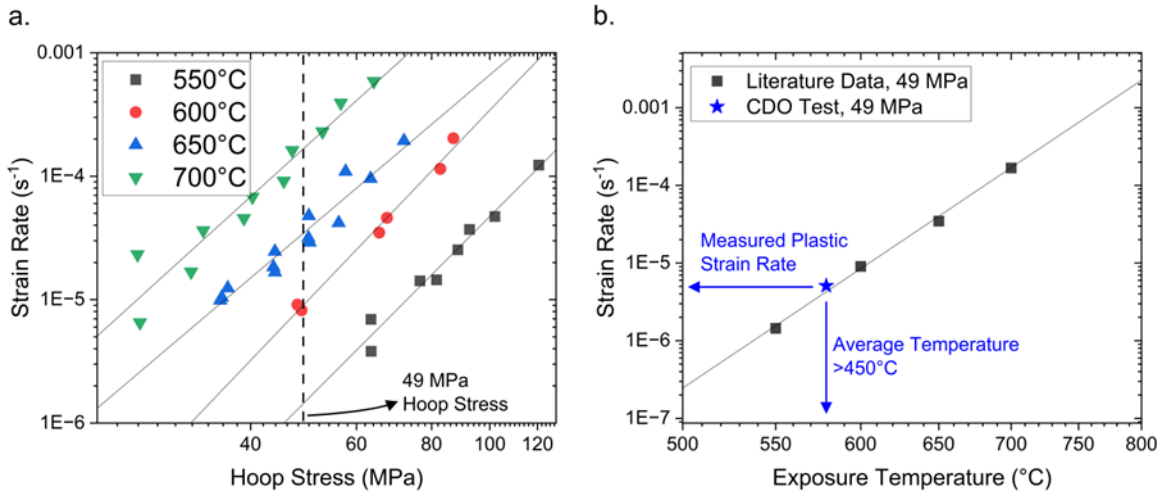

*Figure 7. a. Hoop direction creep data from Bell et. al [11], b. comparison of temperature dependent strain rates at 49 MPa. *300-450°C data was not included in average CDO test sample temperature due to unexpected deformation to occur at lower temperatures.*

3.3 FeCrAl CDO Test with Initial ~45 MPa Hoop Stress

The same analysis procedure as was shown for Zry-4 CDO test will now be explained for FeCrAl alloy C26M2 with a 45MPa hoop stress. Figure 8a shows the temperature profile collected for the FeCrAl CDO test, where the profile in black is the controller temperature readout and the profile in red is saved data from the DIC digital acquisition system (DAQ). Cycles 9-12 and 28-32 are missing data due to software collection issues. As such, analysis will only be performed where strain data is present, as shown in Figure 8b and Figure 8c. Again, cyclic strain response was witnessed from DIC average hoop strain data. Figure 8d shows the first three temperature cycles, where almost all of the strain recorded upon heating was an elastic response to the heating profile. The total strain for FeCrAl after 36 cycles was less than 1%.

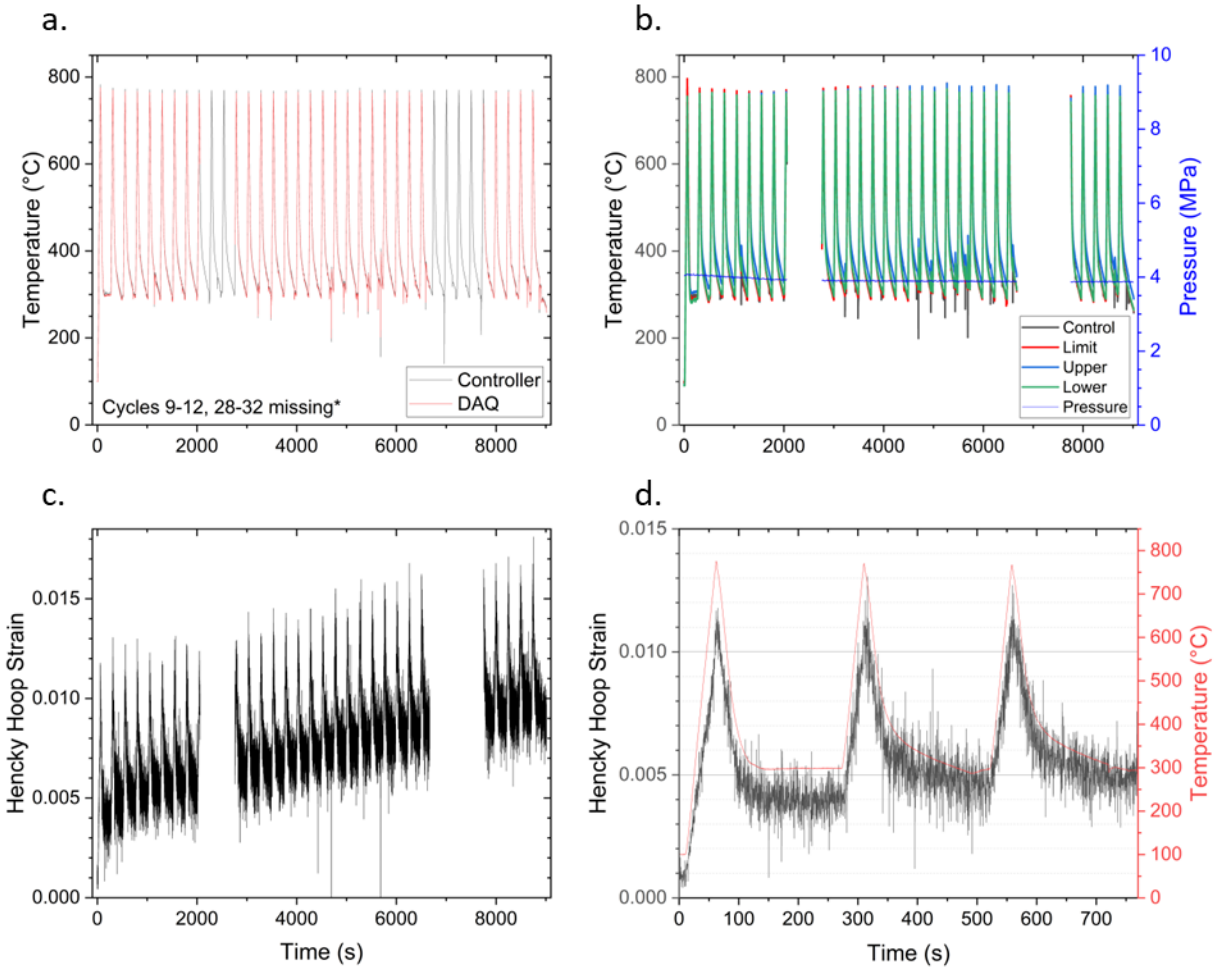

Figure 8. a. Power supply controller and DIC digital acquisition system data output comparison for FeCrAl CDO test, b. full temperature and pressure history where strain data was acquired, c. full strain data of FeCrAl CDO test, and d. temperature and strain curves for the first three temperature cycles.

Each heating and cooling cycle was separated for analysis of thermal expansion, Figures 9a and b. Due to the low strains recorded, noise was higher with the FeCrAl data compared to previously discussed Zry-4. Yet, similar analysis was performed, where thermal expansion was calculated up to 700°C upon heating and from 700 – 400°C upon cooling. The calculated cycle CTEs are shown in Figures 9c and d with a comparison to dilatometry thermal expansion ranges from 300 – 700°C [12]. While general agreement was found between dilatometer CTE data and the CTE calculated during CDO testing, it is clear that the heating cycles showed a preference to lower CTE values while cooling cycles

were generally higher than the baseline dilatometer range. Removing the elastic response, total plastic strain accumulated over each cycle is shown in Figure 10. Strain hardening was evident over the first four cycles, upon which a steady state deformation rate of 5.41×10^{-7} /s was apparent.

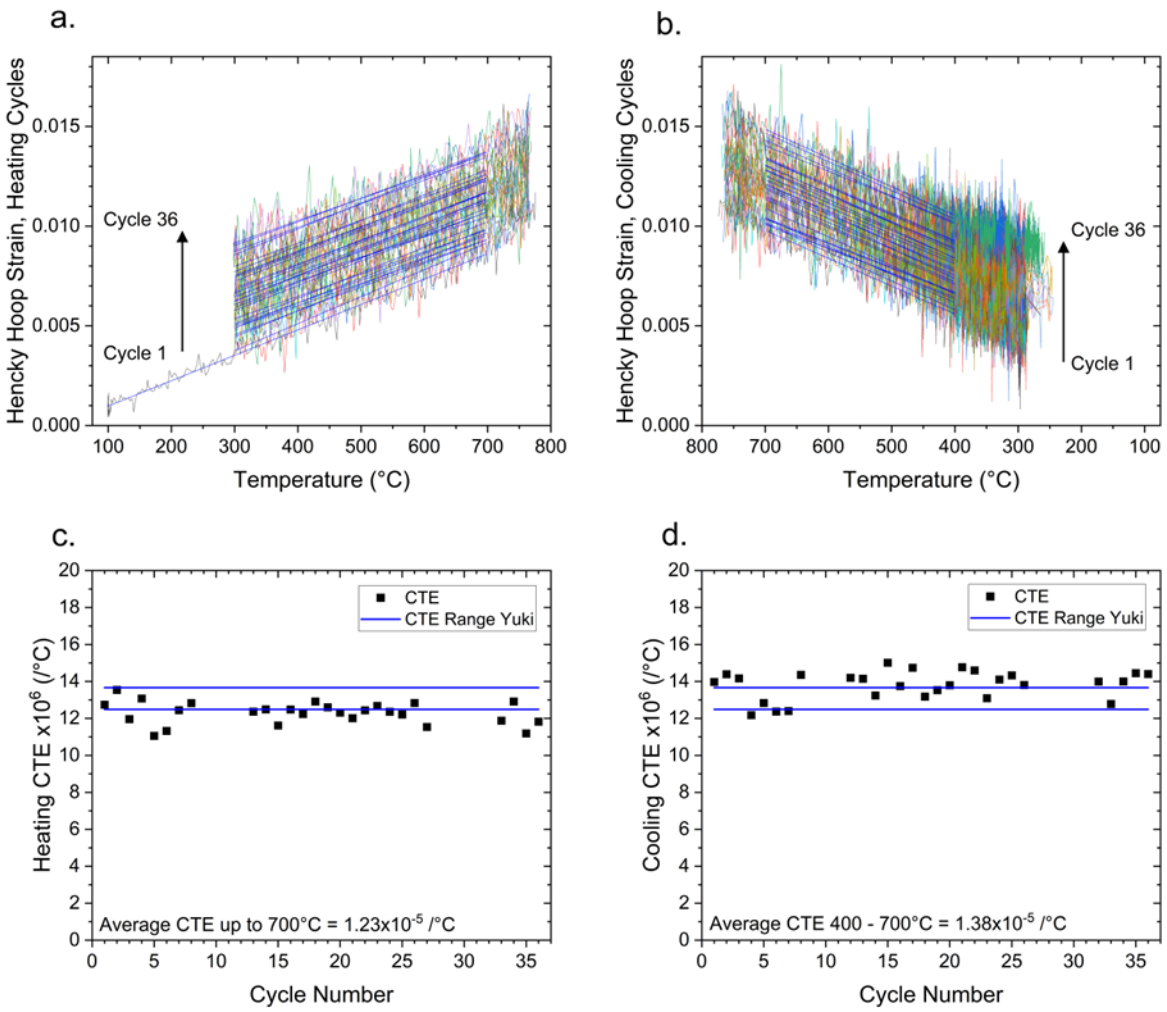

Figure 9. FeCrAl strain profiles separated into heating (a) and cooling (b) cycles, thermal expansion calculation on heating up to 700°C (c) and on cooling from 700 - 400°C (d), compared to literature CTE range for C26M2 by dilatometry [12].

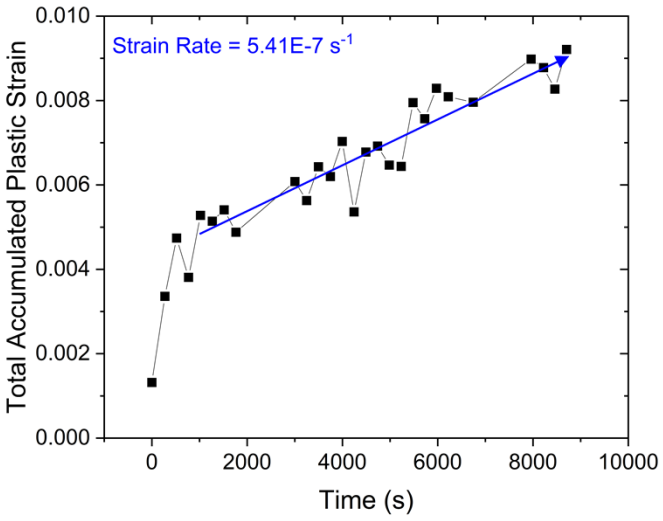

Figure 10. Plastic strain accumulation over each cycle after thermal expansion elastic strains were subtracted from data.

Literature hoop strain rate data was collected from two sources in the temperature range of 480 – 750°C, Figure 11a [11,13]. Limited data is present at lower temperatures for comparable hoop stresses as was performed in this test, and therefore extrapolation was used to estimate a hoop strain rate isotherm at 45 MPa. The isotherm is presented on Figure 11b, where the linear fit was found acceptable given the degree of extrapolation performed. The C26M CDO strain rate was determined from Figure 10, while the average sample temperature was determined by averaging the sample temperature for all times greater than 615°C. The 615°C threshold was chosen to provide similar bounds to the Zry-4 CDO test, as this temperature represented a $1x10^{-8}$ /s strain rate from the linear fit of Figure 11b. It is assumed that visible deformation during the given test times would result from a strain rate greater than $1x10^{-8}$ /s. Therefore, an average sample deformation temperature over the 36 cycles was 701°C. General agreement was again found between the average deformation temperature and simplified creep test data for C26M.

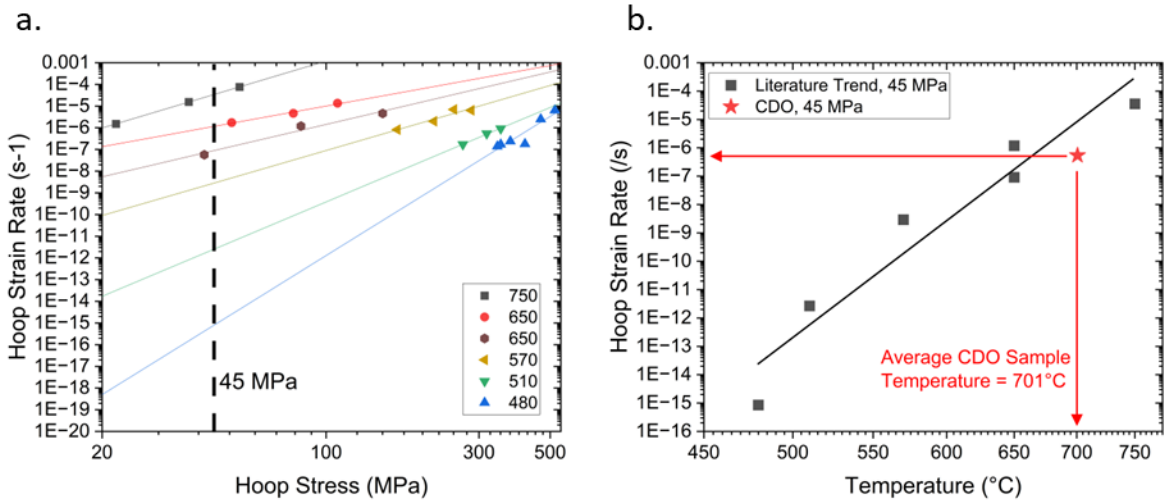

Figure 11. a. C26M strain rate dependence on pressure [11,13], b. isotherm trendline of strain rate data with the CDO test overlaid.

3.4 Zry-2 CDO Test with Initial ~45 MPa Hoop Stress

The Zircaloy-2 cladding segment was exposed to a 45 MPa hoop stress and ruptured midway through the second heating cycle, Figure 12a. Thus, comparable analysis as was done for Zry-4 and C26M could not be completed. The high strains of ~30% on average at the time of rupture allow for analysis of hoop stress evolution during the transient testing. The average hoop strain data is shown in Figure 12b, where high noise was present during the first cooling cycle and second heating cycle. The excess noise was present due to uneven lighting of the specimen, which limited tracking capabilities. Smoothed trends were determined for analysis, which are shown on Figure 12c for each cycle, and the strain derivatives are shown in Figure 12d.

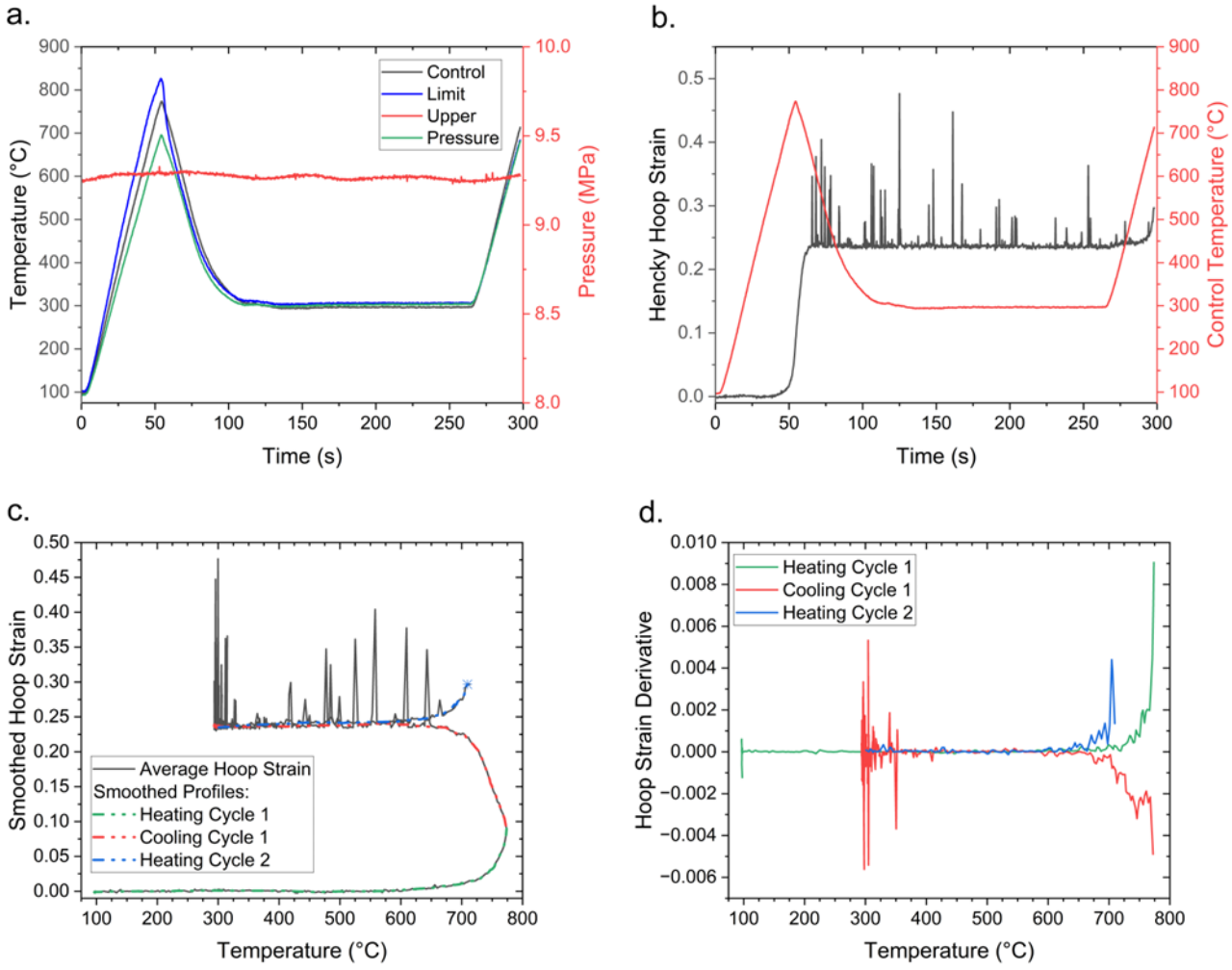

Figure 12. a. Temperature and pressure profile for Zry-2 cycles to 750°C, b. strain accumulation during testing, c. smoothed strain profiles, and d. hoop strain derivatives as a function of sample temperature.

Figure 13 showcases three regimes for each cycle of the Zry2 exposure. The cycles are color coded. The squares represent the strain onset temperature and associated stresses. It can be seen that we start initial deformation at a lower temperature for cycle 1's heating phase, while there is obvious strain hardening for the cooling cycle 1 and heating cycle 2. It makes sense that both these final two cycles show the same strain onset, as no deformation took place during the time at lower temperature between the two datapoints. A 1% strain change datapoint (circles) was also measured for each cycle. Here, both the heating and cooling curve 1 points show similar onset temperatures, although the hoop stress has

changed dramatically due to cladding wall thinning. The third cycle shows a much lower temperature for reaching a 1% strain change, indicative of a rapidly evolving strain rate. Such impacts of heating rate and variable strain rate are likely dependent on the temperature history and the microstructure and therefore warrants further attention.

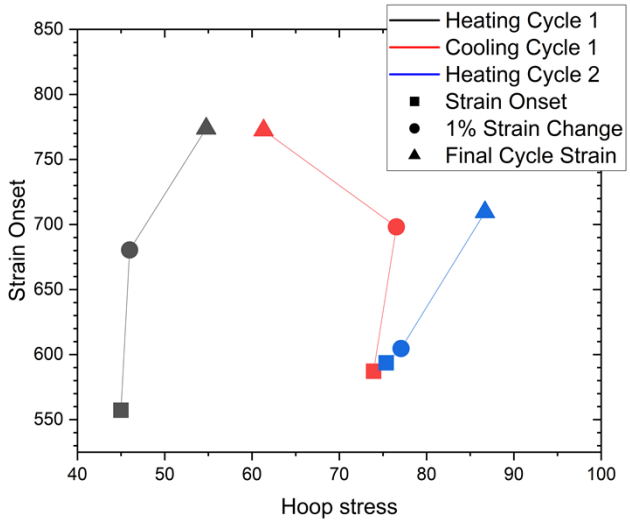

Figure 13. Hoop stress and sample temperature for each cycle; strain onset, 1% strain change, and final cycle strain data are presented.

4. Future Improvements

While reliable strain data can be captured with the region of interest referenced by the closest thermocouple, there remains clear discrepancies in the current furnace heating rates and temperature uniformity. The current limiting factors for controllable heating, including rate and uniformity, are the power output and geometry of the infrared lamp/chamber system in the DIC furnace. “SATS 2” was developed to address these limitations by introducing three times the number of lamps (more coverage) and power (8 kW vs 24 kW), as well as reflective chambers that more uniformly distribute the infrared radiation. For SATS 2, DIC capabilities will be established out-of-cell by removing one of the twelve lamps to create a viewport. As such, it is crucial to thoroughly understand the baseline performance of the new SATS 2 furnace's improvements in heating rate and thermal gradient, before and after modifications are made for DIC.

Preliminary demonstrations of CDO profiles in a FY23 report [14] revealed that SATS 2 offers enhanced transient heating and thermal profiles compared to the previous non-DIC SATS furnace. The previous reports on SATS 2 were published concurrently with development, before the establishment of steam flow and the completion of full controller programming. While CDO testing involves multiple repeated heating profiles, single transient LOCA testing is the most relevant method for qualifying the furnace's performance in its established state. LOCA tests uniquely involves transient heating for which extensive historic data on nuclear fuel cladding is available. To rigorously assess the heating capabilities and associated thermal gradient, Zircaloy-4 cladding segments were subjected to simulated LOCA testing in a steam environment at rates of 1, 5, 25, and 50 °C/s under an internal pressure of 8.3 MPa. The burst properties, along with the geometry of the ballooned region and rupture opening, were evaluated to compare with historical trends. This comparison aims to validate the SATS 2 furnace, which will be deployed with stereo DIC capabilities in the near future.

Figure 14(a) and Figure 14(b) presents the thermocouple readings from for the 1 and 50 °C/s tests, respectively, located 12 mm above the centerline and placed 180° from each other. The "control" thermocouple dictated the furnace output, while the other provided an azimuthal reading. The difference between the two ($T_{control} - T_{azimuthal}$) is also plotted. Generally, lower heating rates resulted in lower thermal gradients, with the maximum difference being 12, 7, 82, and 62 °C for 1, 5, 25, and 50 °C/s testing.

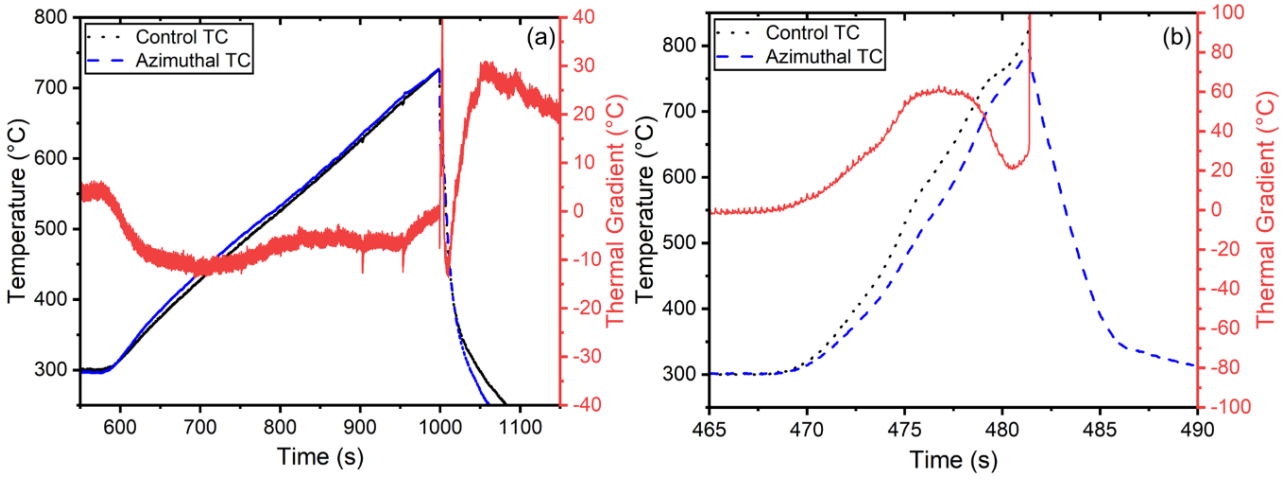

Figure 14. Thermocouple temperature readings and the difference between the azimuthal thermocouples for the test at (a) 1 °C/s and (b) 50 °C/s.

These discrepancies could be related to thermal transport issues associated with the alumina filler rod, first noted during SATS 2 testing in the previous report [14]. The discrepancies may stem from filler rod thermal inertia considerations or contact with the inner cladding wall, altering heat transfer dynamics. For example, if the filler rod contacts one side near a thermocouple, it could asymmetrically skew the heat transport, causing a difference in thermocouple readings. This asymmetry would be exacerbated at higher heating rates considering the limited time for heat transfer to even out the temperature distribution.

While not presented here, a test at a 50 °C/s heating rate was performed on a C26M FeCrAl tubing using a 6 mm filler rod, instead of an 8 mm rod, ensuring no contact with the inner wall. The internal pressure was relatively low (6.2 MPa), resulting in a burst temperature of 1020 °C. The azimuthal thermocouple reading was only a maximum of 12 °C lower than the control reading during the transient. However, the effect of these filler rod changes (increased gas volume) on critical parameters such as balloon morphology and rupture geometry is still being assessed. Future CDO testing, once DIC capabilities are established in SATS 2, could consider using thinner filler rods if rupture geometry and failure are not critical evaluation parameters.

Figure 15 presents the burst temperature and hoop stress for the four tests, alongside curves from the historic Chapman correlation [15–17] for Zircaloys, which is dependent on heating rate. The Chapman correlation accounts for heating rates up to 28 °C/s, beyond which the heating rate dependence saturates, meaning heating rates above 28 °C/s will yield similar burst temperatures. The samples tested at 25 °C/s and 50 °C/s burst at comparable temperatures, showing relative agreement with their respective curves. The 1 °C/s sample also aligned well with the Chapman correlation, while the 5 °C/s test exhibited a burst temperature 30 °C higher than the curve, but still in line with the general trend with heating rate. These results indicate that the SATS 2 furnace, when performing LOCA testing at high heating rates in a steam environment, produces results consistent with historical trends and burst criteria developed using entirely different heating methods and testing apparatus. This demonstrates the fidelity of the transient

conditions produced by this system at higher rates, thereby providing a reliable tool for refining our understanding during CDO testing when stereo DIC is integrated.

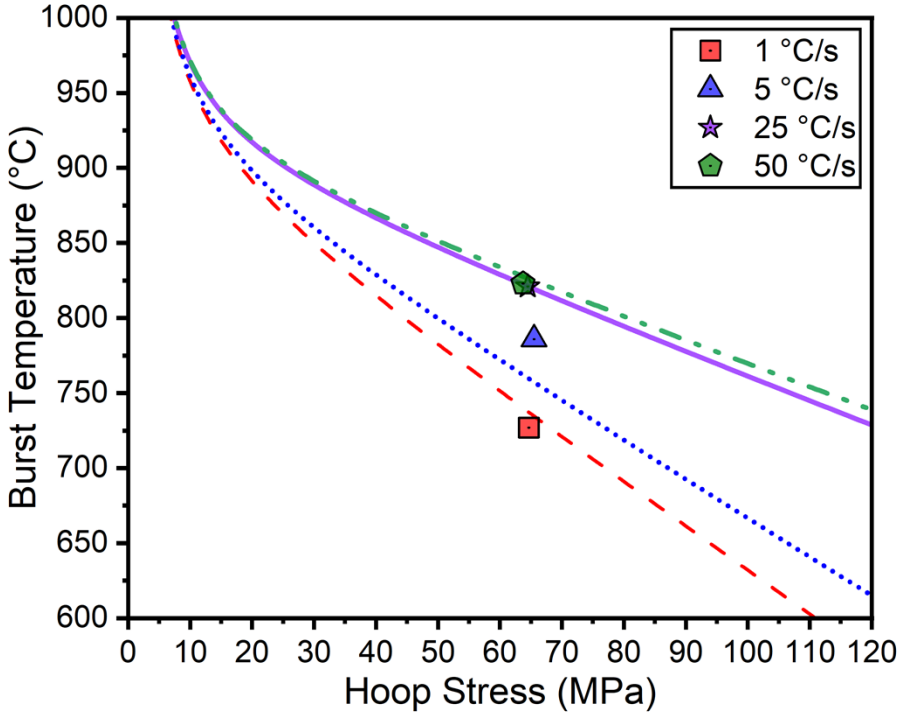

Figure 15. Burst temperature and hoop stress data points compared to historic empirical curves based on heating rate for Zry-4.

Diametric strain, as shown in Figure 16(a), was measured using ImageJ analysis of the images in Figure 16(b) to investigate the trends in balloon morphology with varying heating rates and burst temperatures. Lower maximum diametric strains were observed with slower heating rates, with the 1, 5, 25, and 50 °C/s tests exhibiting strains of 94%, 53%, 37%, and 32%, respectively. These results align with the general trends established over the past 50 years of LOCA burst testing, where slower heating rates result in higher diametric strain [17].

It is important to note that these specimens are not directly comparable, as the burst temperatures varied by over 100 °C. Additionally, the characterization resolution for quantities like diametric strain and burst temperature dependence on heating rate remains crude. The relationship between these variables can be better understood using tools like DIC, which holds significant value for high heating rate LOCA testing as well as CDO.

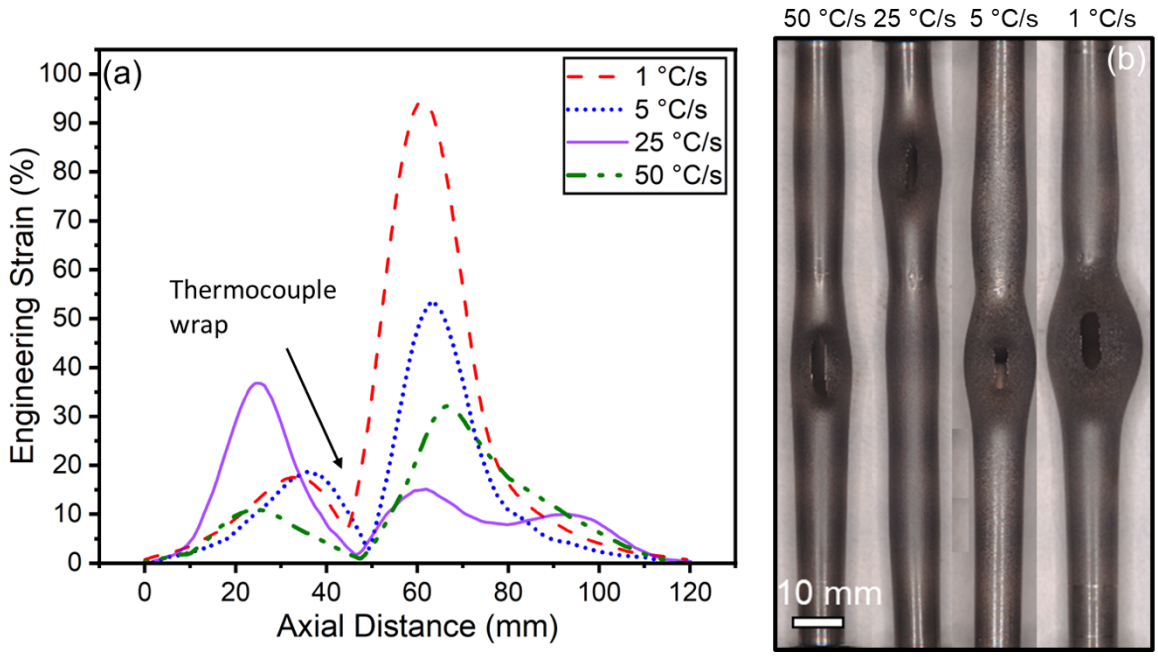

Figure 16. (a) Diametric strain profiles determined from the samples and (b) images of the respective specimen.

Current efforts are underway to outfit the SATS 2 furnace for use with DIC. The electrical interface will be reconfigured from running the lamps in pairs at 480 V to running in series at 240 V and 60 A, allowing for the removal of a single lamp to create a viewport. This will allow for the introduction of DIC to SATS 2 with the least amount of disturbance to the infrared thermal transport infrastructure. This modification will introduce DIC to SATS 2 with minimal disturbance to the infrared thermal transport infrastructure. Although the heating rate and stability of the furnace are expected to be lower than in the fully intact configuration of SATS 2, the improvements in stability, uniformity, and rate will surpass those of the current four-lamp "SATS 1" DIC configuration and the six-lamp SATS 2 DIC setup described by Doyle et al [18].

5. Conclusion

Cyclic dryout testing was performed on Zry-4, C26M2 FeCrAl, and Zry-2 up to 750°C with comparable initial hoop stresses. Zry-4 and C26M2 did not rupture after 36 cycles, while Zry-2 ruptured upon heating during the second cycle, showcasing possible increased susceptibility of Zry-2 to deformation compared to Zry-4 and C26M2. Digital image correlation was used to measure thermal expansion coefficients for heating and cooling cycles, with general agreement to expected literature values. An understanding of the elastic material response during the transients allowed for a clearer visualization of accumulated plastic strain during the tests. For Zry-4 and C26M2, steady state creep rates were found that agree with expected hoop strain rates for a given average deformation temperature throughout the full cyclic events. This result implies that plastic deformation during transients can be predicted and summarized by their average surface temperature. The threshold for defining an average deformation temperature was assumed, and it is clear that further research is needed to better define lower limits where claddings will not experience measurable deformation. Impacts of cyclic dryout and departure from nucleate boiling on cladding deformation are needed for multiple internal pressures to enhance fidelity of fuel performance codes and to establish trends related to potential cladding reuse in BWRs.

6. References

[1] Appendix A to Part 50—General Design Criteria for Nuclear Power Plants, NRC Web (n.d.). https://www.nrc.gov/reading-rm/doc-collections/cfr/part050/part050-appa.html.

[2] T. HARA, S. MIZOKAMI, Y. KUDO, S. KOMURA, Y. NAGATA, S. MOROOKA, Current Status of the Post Boiling Transition Research in Japan: Integrity Evaluation of Nuclear Fuel Assemblies after Boiling Transition and Development of Rewetting Correlations, J. Nucl. Sci. Technol. 40 (2003) 852–861. https://doi.org/10.1080/18811248.2003.9715428.

[3] A. Satou, Y. Wada, Y. Sibamoto, T. Yonomoto, Study on dryout and rewetting during accidents including ATWS for the BWR at JAEA, Nucl. Eng. Des. 354 (2019) 110164. https://doi.org/10.1016/j.nucengdes.2019.110164.

[4] W. Wulff, H.S. Cheng, A.N. Mallen, Causes of instability at LaSalle and consequences from postulated scram failure, Brookhaven National Lab., Upton, NY (USA), 1990. https://www.osti.gov/biblio/6397094.

[5] T. Kozlowski, A. Wysocki, I. Gajev, Y. Xu, T. Downar, K. Ivanov, J. Magedanz, M. Hardgrove, J. March-Leuba, N. Hudson, W. Ma, Analysis of the OECD/NRC Oskarshamn-2 BWR stability benchmark, Ann. Nucl. Energy 67 (2014) 4–12. https://doi.org/10.1016/j.anucene.2013.09.028.

[6] A. Dokhane, O. Zerkak, H. Ferroukhi, I. Gajev, J. Judd, T. Kozlowski, Trace/simulate-3k analysis of the NEA/OECD oskarshamn-2 stability benchmark, in: 16th Int. Top. Meet. Nucl. React. Therm. Hydraul. NURETH 2015, American Nuclear Society, 2015: pp. 4757–4770. https://www.academia.edu/download/81144686/13418.pdf.

[7] K.A. Kane, S.K. Lee, S.B. Bell, N.R. Brown, B.A. Pint, Burst behavior of nuclear grade FeCrAl and Zircaloy-2 fuel cladding under simulated cyclic dryout conditions, J. Nucl. Mater. 539 (2020) 152256. https://doi.org/10.1016/j.jnucmat.2020.152256.

[8] M. Ridley, C. Massey, S. Bell, N. Capps, High temperature creep model development using in-situ 3-D DIC techniques during a simulated LOCA transient, Ann. Nucl. Energy 193 (2023) 110012. https://doi.org/10.1016/j.anucene.2023.110012.

[9] J.D. Hales, S.R. Novascone, B.W. Spencer, R.L. Williamson, G. Pastore, D.M. Perez, Verification of the BISON fuel performance code, Ann. Nucl. Energy 71 (2014) 81–90. https://doi.org/10.1016/j.anucene.2014.03.027.

[10] K. Geelhood, W. Luscher, L. Kyriazidis, C. Goodson, J. Corson, MatLib-1.0: Nuclear Material Properties Library, (2021).

[11] S. Bell, Toward Accelerated Qualification of ATF Claddings: An In-Situ Burst Testing Framework and Insights into Zr Alloy LOCA Behavior, Dr. Diss. (2023). https://trace.tennessee.edu/utk_graddiss/9050.

[12] Y. Yamamoto, K. Kane, B. Pint, A. Trofimov, H. Wang, Report on Exploration of New FeCrAl Heat Variants with Improved Properties, Oak Ridge National Laboratory (ORNL), Oak Ridge, TN (United States), 2019. https://doi.org/10.2172/1558505.

[13] P. Joshi, B. Kombaiah, M.N. Cinbiz, K.L. Murty, Characterization of stress-rupture behavior of nuclear-grade C26M2 FeCrAl alloy for accident-tolerant fuel cladding via burst testing, Mater. Sci. Eng. A 791 (2020) 139753. https://doi.org/10.1016/j.msea.2020.139753.

[14] S. Bell, N. Capps, M. Ridley, D. Sweeney, J. Harp, A. Willoughby, Y. Yan, K. Linton, SATS Enhanced Capabilities and Demonstration of Improved Ramp Rates for In-Cell Testing, Oak Ridge National Laboratory, 2023.

[15] R. Chapman, J. Crowley, A. Longest, G. Hofmann, Zirconium Cladding Deformation in a Steam Environment with Transient Heating, in: J. Schemel, T. Papazoglou (Eds.), Zircon. Nucl. Ind., ASTM International, 100 Barr Harbor Drive, PO Box C700, West Conshohocken, PA 19428-2959, 1979: pp. 393-393–16. https://doi.org/10.1520/STP36692S.

[16] R.H. Chapman, Multirod Burst Test Program progress report, July--December 1977. [BWR; PWR], Oak Ridge National Lab., Tenn. (USA), 1978.

[17] D.A. Powers, R.O. Meyer, Cladding Swelling and Rupture Models for LOCA Analysis, US Nucl. Regul. Comm. (1980).
[18] P. Doyle, M. Ridley, S. Bell, J. Harp, N. Capps, B. Johnston, A. Willoughby, M. White, Digital Image Correlation Strain Mapping on the In-cell Severe Accident Test Station Readiness Assessmen, Oak Ridge National Laboratory, 2024.